Modelling temporal changes in the gravity field in the Nankai Trough Subduction Zone, Japan

S. C. Vassvåg[1,2], K. Atakan[1], M. Lien[2], S. Kodaira[3], T. Fujiwara[3]

[1]Department of Earth Science, University of Bergen, Bergen, Norway
[2]MonViro AS, Bergen, Norway
[3]Research Institute for Marine Geodynamics, Japan Agency for Marine-Earth Science and Technology (JAMSTEC), Yokohama, Japan

Key Points:

- Seafloor gravimetry is evaluated as a method for monitoring processes leading to shallow slow earthquakes in the Nankai Trough
- Fluid volumes are modelled within regions corresponding to slow earthquake locations off the Kii Peninsula, Japan
- A time-lapse gravity signal can be used to determine the lateral extent of density changes, indicating where these changes occur

Corresponding author: Siri Catherine Vassvåg, `siri.vassvag@monviro.com`

Abstract

Monitoring slow earthquake activity in subduction zones can give important insight into the stress build-up and subsequent rupture extent of megathrust earthquakes. Extensive slow earthquake activity occurs up-dip of the seismogenic zone of the Nankai Trough subduction zone, an area that might be awaiting a large ($M_w \geq 8$) earthquake in the near future.

Mechanisms used to explain the occurrence of slow earthquakes are often linked to temporal changes in fluid transport along faults. This study utilises this theory in evaluating the usage of 4D gravity measurements on the seafloor for monitoring changes in fluid flow, hence monitoring the slow earthquake activity and the mechanisms behind them. We model the gravity response from fluid-related density changes in an area of the Nankai Trough accretionary prism that experiences several slow earthquake episodes in the interseismic period.

The forward modelled 4D gravity response is used to estimate volumes of fluid at specific locations of the accretionary prism and plate interface corresponding to a minimum gravity signal of 5 μGal. This accuracy in the gravity signal is obtainable through technology monitoring micro-gravity effects at the seafloor. Based on the results we have formulated a hypothesis on how small fluid volume changes can be detected through a gravimetry survey at the seafloor of the Nankai Trough. The results can also be used to design a survey layout for obtaining valuable 4D gravity data at the Nankai Trough.

Plain Language Summary

This study evaluates the use of gravity monitoring of earthquake activity in the Nankai Trough subduction zone, an area experiencing large earthquakes. Fluid movement within the subsurface is assumed to relate to the rupture of smaller earthquakes here, causing density changes surrounding the earthquakes. A modelling study has been conducted based on the location of these earthquakes, where changes in gravity are modelled through changes in the density of the subsurface rocks. The study can be used to define a layout of measurement points for monitoring gravity changes at the Nankai Trough, using sensitive instrumentation to detect gravity changes at the seafloor. By mapping these small earthquakes, a deeper understanding of the stress build-up in the faults of the subduction zone can be acquired, further contributing to earthquake research in the area.

1 Introduction

The need for a deeper understanding of earthquake rupture processes was highlighted following the M_w 9 Tohoku earthquake that struck northern Japan in 2011, rupturing an unexpectedly large fault section near the trench (Satake, 2015). Following this earthquake, the focus was moved to the Nankai Trough subduction zone of southwestern Japan, which, as fig. 1 indicates, has been experiencing significantly less activity during the interseismic period. Large megathrust earthquakes of M_w 8 occur here every 100-200 years (Linde & Sacks, 2002), rupturing large segments of the plate interface and often causing devastating tsunamis (Ando, 1975; Satake, 2015). According to the Japan Agency for Marine-Earth Science and Technology (JAMSTEC), within the next 30 years, there is a 60% chance that a new megathrust earthquake will occur in the Nankai Trough (Kawaguchi et al., 2015), an estimate that has increased the interest in research about this subduction zone. Locating patches of strongly coupled asperities (Kanamori, 1971) along the plate interface is of importance to estimate the rupture extent of megathrust earthquakes.

Contrary to regular earthquakes, extensive slow earthquake activity is observed within the Nankai Trough accretionary prism (Obara & Ito, 2005; Takemura et al., 2019). These are earthquakes with longer rupture times, or lower dominant frequency signals than reg-

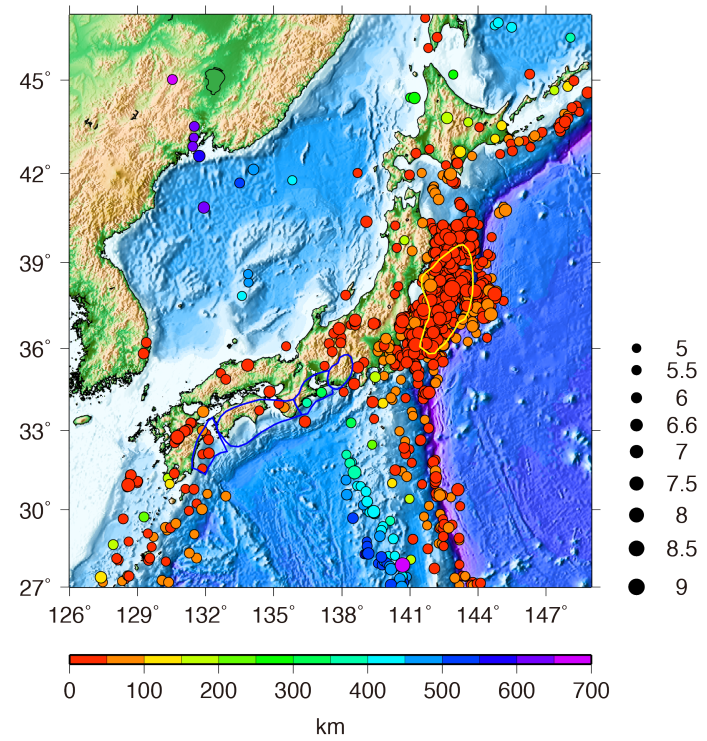

Figure 1. Seismicity in Japan between January 2011 and December 2017. The radius of the circles represents the magnitude of the events as indicated in the legend, and the events are all of magnitude 5 and higher. The hypocentre estimates are retrieved from The Headquarters for Earthquake Research Promotion (2020). The blue outlines over the Nankai Trough indicate, from right to left, fault slip models of the Tokai, Tonankai, Nankai and Huyga-Nada megathrust earthquakes (Ariyoshi et al., 2014). The yellow outline over the Japan trench indicates the fault slip model of the 2011 Tohoku earthquake (Ozawa et al., 2011).

ular earthquakes (Linde & Sacks, 2002; Beroza & Ide, 2011). An important aspect of slow earthquakes is that their rupture may influence megathrust earthquakes by increasing or reducing the stress applied to plate interface asperities, as well as affecting the possible rupture extent of megathrust earthquakes (Ito et al., 2007; Beroza & Ide, 2011). Increasing our knowledge on processes leading to slow earthquakes will contribute also to enhance our understanding of great earthquakes at the Nankai Trough.

An important process assumed to influence earthquake rupture is fluid flow within fault rocks. An increase in pore pressure due to water influx can reduce the frictional strength of a fault plane or lead to lowering of the stress needed to trigger an earthquake (Engelder & Price, 1993; Stein et al., 2003). The mechanisms leading up to the rupture of slow earthquakes are not so well known, but pressure build-up caused by fluid flow is likely to be an important factor here as well (Shelly et al., 2006).

Using seismometers in the DONET1 network off the coast of the Kii Peninsula, Tonegawa et al. (2017) identified zones of low seismic velocities, and Araki et al. (2017) observed localised pore pressure changes, both effects assumed to be related to slow earthquakes. Considering our limited knowledge of the flow of fluid within the Nankai Trough frontal thrust, seafloor gravimetry has been proposed as a method to identify the lateral extent of mass changes leading to these events, in particular mapping where excess fluids might be located. Through the Accurate Seafloor Subduction Zone Monitoring (ASUMO) project, the Norwegian company MonViro is planning to apply methods previously used to monitor fluid changes in hydrocarbon reservoirs (Agersborg et al., 2017), for this purpose.

Large crustal density changes have been detected before regular earthquakes through ship-borne gravimetry and GRACE data (Tomoda, 2010; Tsuboi & Nakamura, 2013; Panet et al., 2018). However, smaller density changes are expected relating to slow earthquakes, making it necessary to increase the sensitivity in the data by performing measurements closer to the region of interest with orders of magnitude higher accuracy than what is currently available using other gravity methods. This is achieved through seafloor gravimetric measurements, which have been successful in measuring 4D gravity changes to resolutions down to 1 μGal (10^{-8} m/s^2) (Ruiz et al., 2016, 2020).

Through this research, we study the feasibility of using seafloor gravimetry to detect density changes within the Nankai Trough accretionary prism, with a specific focus on tectonic processes and fluid flow related to slow earthquakes. The analysis is based on forward modelling of the 4D gravity response from different fluid flow scenarios linked to slow earthquakes, to assess the ability to map density changes in the subsurface through a gravimetric survey. The purposes of our modelling are twofold. First, identify regions where fluid-induced density changes could occur and assess the magnitude of the resulting 4D gravity change. Secondly, to provide input for the design of a seafloor gravimetric experiment at the Nankai Trough.

2 Nankai Trough Subduction Zone

At the Nankai Trough, the Philippine plate subducts below the Amurian plate at an approximate rate of 2-4 cm/yr (Seno et al., 1993). The low subduction rate combined with the Philippine plates relatively young age of 26-15 Ma (Okino et al., 1994) leads to a low subduction angle, and a large, coupled region between the plates (Ruff & Kanamori, 1983). Based on slip inversion of megathrust earthquakes that occurred along the plate interface in the Nankai Trough, locations of several large asperities have been revealed. However, in the shallower parts of the plate interface, identifying locations of possible smaller asperities is difficult due to the low resolution of the inversion results (Yokota et al., 2016; Noda et al., 2018). Over the last decade, these shallow regions have been subject to several episodes of slow earthquake activity (Obara & Ito, 2005; Takemura et al., 2019).

Slow earthquakes are thought to occur due to the rupture of small asperities (Lay & Kanamori, 1981), with varying mechanisms suggested as triggers for these earthquakes (Saffer & Wallace, 2015; Bürgmann, 2018). In our research, we study the distribution of shallow very-low-frequency earthquakes (VLFEs) in more detail, specifically events detected in clusters around the DONET1 network defined by Nakano et al. (2016, 2018). Studies by Kodaira et al. (2004) and Araki et al. (2017) indicate localised regions of high pore fluid pressure coinciding with areas of slow earthquake activity, and Saffer and Wallace (2015) suggest fluid dynamics as a triggering mechanism behind these slow earthquakes. Hirose et al. (2021) identified aquifers of overpressured water near areas experiencing significant slow earthquake activity off the Shikoku Island region of the Nankai Trough. Based on these various studies, clusters of VLFEs are thought to represent regions where mass changes due to fluid dynamics are likely to occur and are therefore used to constrain our modelling region.

Within the Shikoku basin of the Philippine plate, a nearly 1.5 km thick sediment section is introduced into the subduction zone (Sugimura & Uyeda, 1973). Some sediments are subducted along with the Philippine plate, creating a thick underthrust sediment section below the accretionary prism (Sugimura & Uyeda, 1973; Ike et al., 2008), likely bringing ocean water into the subduction zone. The low permeability of the oceanic sediments at the top of this layer is thought to contribute to trapping the water in the section as it subducts (Tsuji et al., 2008). Mineral dehydration has also been proposed as a source of increased fluids within the Nankai Trough (Saffer & Wallace, 2015). These fluids introduced in the system may be trapped within volumes by impermeable structures, causing the pore pressure increase suggested as a process behind earthquake rupture (J. C. Moore & Vrolijk, 1992; Ike et al., 2008).

3 Data and Methods

The first step in our modelling was defining a geological model and density distribution of the subsurface building on a detailed 3D P-wave velocity structure covering the Kii Peninsula region of the Nankai Trough (Nakanishi et al., 2018). We then set up scenarios for the 4D gravity modelling building on information on the geology and seismic activity in the area (Nakano et al., 2018), computing the gravitational effects at the seafloor from fluid-induced density changes in the subsurface. The gravity response was computed using the GravMod modelling tool (MonViro, 2019).

3.1 Creating the density map

To obtain a density map of the subsurface, a geological model describing the layering and individual rock properties is required.

3.1.1 Geological model

We used a section of the 3D P-wave velocity model to set up the geological model, covering the Kii Peninsula region of the Nankai Trough down to 60 km depths. This velocity model was created by Nakanishi et al. (2018) through a combination of data from several seismic surveys and long-term ocean-bottom seismic measurements. The data resulted in a highly detailed, densely spaced velocity structure of the Nankai Trough, revealing the location of the subducted Philippine plate and details on the layering of the subsurface.

Based on the 3D velocity structure and supporting material on the geological properties of the region, ten subsurface geological layers were identified covering both the subducting Philippine plate and the overriding crust of the Amurian plate. Each layer is defined by an individual velocity range within the 3D velocity model.

Figure 2a shows a cross-section of the 3D velocity model, and the division of layers in the geological model is illustrated in fig. 2b. The Philippine plate section was modelled by three layers (layers 8-10 in fig. 2b) where layer 10 is the upper mantle, defined as peridotite, layer 9 is defined as gabbro and layer 8 as basalt. This structure follows the typical layering of oceanic crust (Kearey et al., 2009). A thick sediment section is also subducting along with the Philippine plate (Sugimura & Uyeda, 1973; Ike et al., 2008). Since the P-wave velocities of this layer are similar to the sedimentary sections above, these underthrust sediments were included in the composition of the accretionary prism layers in the Amurian plate crustal model (layers 1-3 in fig. 2b).

The Amurian plate consists of a young accretionary prism with variable sedimentary composition and an upper crust assumed to include an ancient accretionary prism, the Shimanto geological belt (Taira et al., 1992). We separated the young accretionary prism into three sedimentary layers, based on layering proposed by Nakanishi et al. (2002). Through studying drill reports from various drilling expeditions of the Integrated Ocean Discovery Program (IODP), performed in connection with the NanTroSEIZE project (JAMSTEC, 2019), we were able to determine properties of the uppermost layers of the model. We defined the first sedimentary section, layer 1, as clay-rich, unconsolidated sediments and layer 2 as mudstone (Kinoshita et al., 2012). Layer 3 was defined as sandstone, based

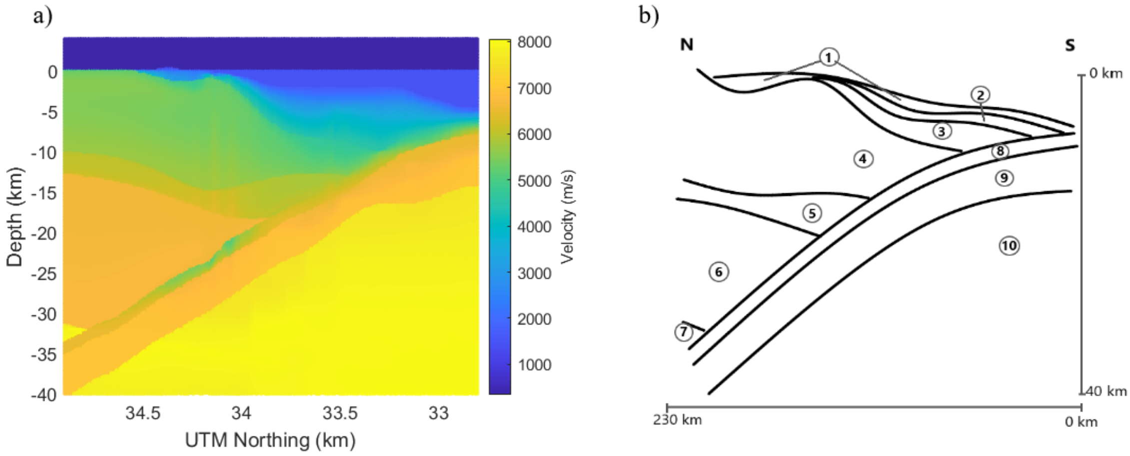

Figure 2. (a) Cross-section of the 3D P-wave velocity model, taken at 136.5°E. The cross-section indicates the distinct layers found in the velocity structure. The layers with velocities around 1000 m/s and below are the air and ocean layer. (b) The 10 layers of the geological model. Layers 1-7 are part of the overriding crust, and layers 8-10 are the subducting crust. Each layer corresponds to specific velocity ranges within the 3D velocity structure by Nakanishi et al. (2018).

on the downwards coarsening of turbidite deposits, which are extensively found at the trough off the Kii Peninsula (Ike et al., 2008).

Studies of the Shimanto belt by Taira et al. (1982) were used to constrain the composition of the upper crust, layer 4. Taira et al. (1982) defined four layers in the Shimanto belt, while we simplified to one rock type, limestone, to define the whole layer. The lower layer of the Shimanto belt is basaltic (Taira et al., 1982), which was used along with studies of typical island arc crust composition (Calvert, 2011) to define layer 5. Research by Calvert (2011) also indicated that the lower crust, layer 6, could be defined by gabbro, and the upper mantle, layer 7, as peridotite.

3.1.2 P-wave velocity to density conversion

The conversion factor between P-wave velocities (v_p) and densities (ρ) building on the equation for P-waves through an isotropic, homogeneous medium, as stated by Mussett and Khan (2000), is defined in eq. 1:

$$\rho_{ij} = \alpha_i v_{p,ij}, \quad \text{where,} \quad \alpha_i = \frac{K_i + \frac{4}{3}\mu_i}{\overline{v_{p,i}}^3}. \tag{1}$$

Here, i=1:I, where I is the number of layers defined in the geological model, and j=1:J, where J is the number of individual velocity values covered by that specific layer. The variables K_i and μ_i are the effective bulk and shear modulus of the medium in the i'th layer, and $\overline{v_{p,i}}$ is the average value of the predefined velocity interval of the same layer. The j'th velocity value in the layer is mapped to a density value using these layer properties, as detailed in Table 1. The conversion factor implicitly accounts for the decreasing porosity with depth as represented by the v_p model while allowing for the use of average rock properties within each layer.

The Hashin-Shtrikman upper bounds for bulk and shear modulus of a linear, elastic, homogeneous medium were used to define the effective bulk and shear modulus of the medium in each layer (Mavko et al., 2009). These bounds are defined by the elastic moduli of the mineral composition of the solid medium (K_m and μ_m), its porosity (ϕ) and the elastic moduli of the constituent in the pore space (K_f and μ_f), in this case, water. The effective bulk and shear modulus of each layer were computed using eq. 2a,b (Mavko et al., 2009):

$$K_i^{HS^+} = \left[\frac{\phi_i}{K_f + \frac{4}{3}\mu_{max,i}} + (1-\phi_i)\sum_{k=1}^{I}\frac{f_k}{K_{m,ik} + \frac{4}{3}\mu_{max,i}}\right]^{-1} - \frac{4}{3}\mu_{max,i}, \tag{2a}$$

$$\mu_i^{HS^+} = \left[\frac{\phi_i}{\mu_f + \zeta(K_{max,i},\mu_{max,i})} + (1-\phi_i)\sum_{k=1}^{I}\frac{f_k}{\mu_{m,ik} + \zeta(K_{max,i},\mu_{max,i})}\right]^{-1} - \zeta(K_{max,i},\mu_{max,i}), \tag{2b}$$

where,

$$\zeta(K_{max,i},\mu_{max,i}) = \frac{\mu_{max,i}}{6}\left(\frac{9K_{max,i} + 8\mu_{max,i}}{K_{max,i} + 2\mu_{max,i}}\right).$$

The variable f_k is the fraction of each mineral found in the medium. For simplicity, either one or two minerals were chosen to define each medium, and f_k=0.5 was chosen as the fraction of each mineral in the dimineralitic rocks.

The mineral compositions and property values chosen for each rock type were based on published values of rock compositions in the Nankai Trough and generic values related to the individual rock types (Bray & Karig, 1985; Carlson & Herrick, 1990; Kehew, 1994; Screaton et al., 2009; Kinoshita et al., 2012; Schön, 2015; Underwood & Song, 2016). The rock properties in the layers of the geological model are summarised in Table 1.

For the deeper layers, the actual values of porosity and the mineral composition are not possible to determine by direct observations. In the peridotite, gabbro and basalt layers, the properties partially needed to be defined by considering how realistic the converted density values were. Therefore, the uncertainty in the densities in these layers is the highest. The densities have been compared to results by Barton (1986), based on empirical relations between P-wave velocities and densities by Ludwig et al. (1970). The comparison shows that only a subset of the computed density values lie outside of the empirical density ranges given by Barton (1986) for the velocity ranges of each layer. At most, 35.5% of the computed densities in the peridotite layer lie beyond the range of the empirical values, reflecting uncertainties in the properties chosen for this layer. The other layers have between 0.2% and 28.7% of the computed densities outside of the empirical ranges. This comparison indicates the uncertainties in the computed density values compared to the empirical values.

Figure 3 shows the velocity cross-section (left) compared to the density mapping (right). Some imperfections in the layering of the density map are present in the deeper layers. This is caused by difficulties in distinguishing the velocity values from each other in parts of the interface between the upper layer of the subducting plate and the layers of the overriding plate. This involves mainly the deeper layers and does therefore not have any negative impact on the modelling.

Table 1. Composition of layers in the geological model defining the Amurian island arc crust (1-7) and the Philippine oceanic crust (8-10). The velocity values are the predefined velocity intervals for each layer, and the densities are given after the conversion of P-wave values from the 3D velocity model. The layers without a source for porosity have not been sampled through ocean bottom drilling. These were therefore determined through tests on how the computed densities responded to porosity changes. The values shown here gave the best fit to average density values for the rock types, proposed by Schön (2015) and Mussett and Khan (2000). The bulk and shear modulus of the minerals from this table were found in Schön (2015) and used in the computation of Hashin-Shtrikman upper bounds for bulk and shear moduli.

Layer	Rocktype	Mineral	Porosity (%)	Velocity (m/s)	Density (kg/m^3)
1	Oceanic sediment	Clay[a]	70[a,b]	1600 - 2046	1760 - 2251
2	Mudstone	Smectite, Illite[c,d]	55[a]	2046 - 3115	1674 - 2549
3	Sandstone	Feldspar[e]	25	3115 - 4700	1752 - 2643
4	Limestone	Calcite[e]	25	4700 - 5800	2209 - 2726
5	Basalt	Augite, feldspar[e]	5	5800 - 6349	2403 - 2631
6	Gabbro	Augite[e]	10	6349 - 7200	2832 - 3034
7	Peridotite	Olivine[e]	10	7200 - 8177	3182 - 3468
8	Basalt	Augite, feldspar[e]	15[f]	4520 - 6439	2215 - 3111
9	Gabbro	Augite[e]	10	6349 - 7200	2832 - 3123
10	Peridotite	Olivine[e]	10	7200 - 8177	3181 - 3429

[a] Screaton et al. (2009); [b] Bray and Karig (1985);
[c] Kinoshita et al. (2012); [d] Underwood and Song (2016);
[e] Kehew (1994); [f] Carlson and Herrick (1990)

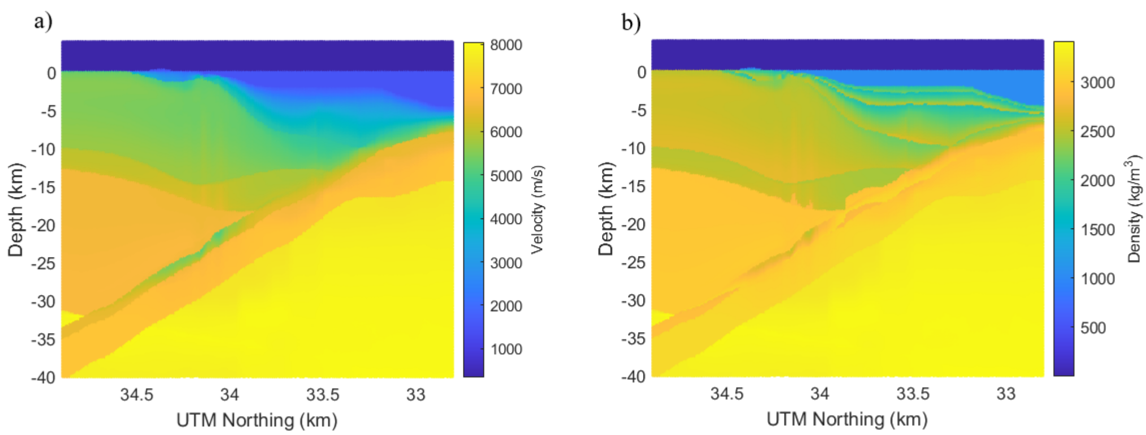

Figure 3. (a) Velocity layering, as shown in fig. 2. (b) Density mapping of velocities at the same transect as the velocity cross-section.

3.2 Forward modelling of gravity

The forward modelling was done using the GravMod modelling tool (MonViro, 2019), utilising analytical expressions for the attraction of a 3D distribution of rectangular prisms. The lateral extent of each prism, Δx and Δy, was chosen to give a good lateral resolution of the density distribution in the area. The vertical extent of each prism was defined by parsing through depth profiles in the density map. Starting at the top of the first layer, an initial density was chosen for each prism, $\rho(z_{min})$, and the interval of subsequent densities within $\pm$ 5% of this initial density and within $\pm$ 1% of each neighbour was assigned to the same prism. Once reaching a depth where one of these thresholds are exceeded, this density value, $\rho(z_{max})$, ends the group, and the final density at the centre of the prism is given by the average density across the given interval. The discretisation follows the layering defined in Section 3.1.1, and prisms do not cross layer boundaries.

Figure 4 illustrates the prisms used for the forward modelling, where x_{min}, x_{max}, y_{min}, y_{max}, z_{min} and z_{max} refer to the corner coordinates of the prism. This discretisation of the density distribution into volume elements gives a good representation of the density structure of the subsurface while reducing the numerical cost of the forward modelling.

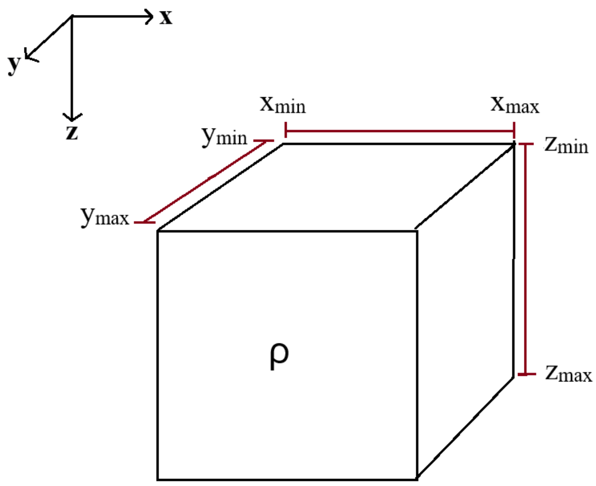

Figure 4. Illustration of a rectangular prism used to discretise the density map. The coordinates for the corners are given by the predefined lateral extent (Δx and Δy). The vertical coordinates are defined by directly using the density vs depth profiles of the density map. An initial density and corresponding depth is chosen (z_{min}), and densities within a given threshold from this initial density are chosen until the threshold is reached at the depth z_{max}. The density ρ of the prism is the average density within the depth range.

Using Newton's law of gravity, the gravitational attraction (δg_{ln}) at the measurement point P_l at the seafloor, located in (x_l,y_l,z_l), from an individual prism with density ρ_n and corner coordinates as illustrated in fig. 4, can be computed following the analytical expression in eq. 3:

$$
\begin{aligned}
\delta \mathsf{g}_{ln} = G\rho_n \int_{z_{n,min}-z_l}^{z_{n,max}-z_l} \Bigg[& \tan^{-1}\left(\frac{(x_{n,max}-x_l)(y_{n,max}-y_l)}{z_n\sqrt{(x_{n,max}-x_l)^2+(y_{n,max}-y_l)^2+z_n^2}}\right) \\
& -\tan^{-1}\left(\frac{(x_{n,min}-x_l)(y_{n,max}-y_l}{z_n\sqrt{(x_{n,min}-x_l)^2+(y_{n,max}-y_l)^2+z_n^2}}\right) \\
& -\tan^{-1}\left(\frac{(x_{n,max}-x_l)(y_{n,min}-y_l)}{z_n\sqrt{(x_{n,max}-x_l)^2+(y_{n,min}-y_l)^2+z_n^2}}\right) \\
& +\tan^{-1}\left(\frac{(x_{n,min}-x_l)(y_{n,min}-y_l)}{z_n\sqrt{(x_{n,min}-x_l)^2+(y_{n,min}-y_l)^2+z_n^2}}\right)\Bigg] dz_n
\end{aligned}
\tag{3}
$$

In eq. 3, $l = 1 : L$ is the number of surface measurement points, and $n = 1 : N$ is the number of prisms used for the computation. The equation integrates over z_n, defined by the vertical extent of the n'th prism and its distance from the measurement point. The aggregated gravity response at P_l from N prisms is then given by $\delta \mathsf{g}_l = \sum_{n=1}^{N} \delta \mathsf{g}_{ln}$.

3.3 4D gravity modelling

For the 4D gravity modelling, we emphasised areas with fluid inflow, leading to pressure build-up and increasing porosity. The pore expansion due to pressure build-up gives a net fluid volume and mass increase with a corresponding 4D gravity response at the seafloor. The modelling assumes that the mass in the surrounding areas remains constant within the considered time frame. Locations of shallow VLFEs in the Nankai Trough were used to decide where the density changes would occur, under the assumption that fluid flow in these regions could trigger slow earthquake episodes (Kodaira et al., 2004; Ito & Obara, 2006). The seismic catalogues by Nakano et al. (2016, 2018), retrieved from the Slow Earthquake Database (Kano et al., 2018), indicate that a significant number of the VLFEs occurred at the plate interface and within the accretionary prism, motivating our choice of modelling scenarios.

Two scenarios were chosen to represent density changes in the Nankai Trough:

1. Fluid flow along the plate interface
2. Fluid flow at slow earthquake locations

The target area for the 4D modelling is illustrated in fig. 5, showing regions where fluid-related mass changes are thought to occur near the trough. The assumption behind the modelled mass changes in these two scenarios is that an increase of fluid within the fault rocks causes a total volume increase of the pore space. The fluid volume increases when flowing water is trapped by impermeable sections of the subsurface (J. C. Moore & Vrolijk, 1992), resulting in increased pore pressure and elastic pore expansion. The pressure build-up eventually causes cracking or faulting of the rocks, triggering the slow earthquake episodes (Engelder & Price, 1993; Bürgmann, 2018). Assuming constant rock compressibility and uniform pressure build-up, the volume expansion is uniform across the fault sections.

The magnitude of the mass change is chosen such that the maximum gravity signal at the seafloor reaches 5 μGal. This threshold is chosen as a conservative measure of the anticipated accuracy in the 4D gravity data at the Nankai Trough, considering various uncertainties affecting the accuracy of seafloor gravimetry (Agersborg et al., 2017; Ruiz et al., 2020).

Vertical movement of the seafloor and changes in the water column and atmosphere above the measurement area will all contribute to the uncertainty of the measured grav-

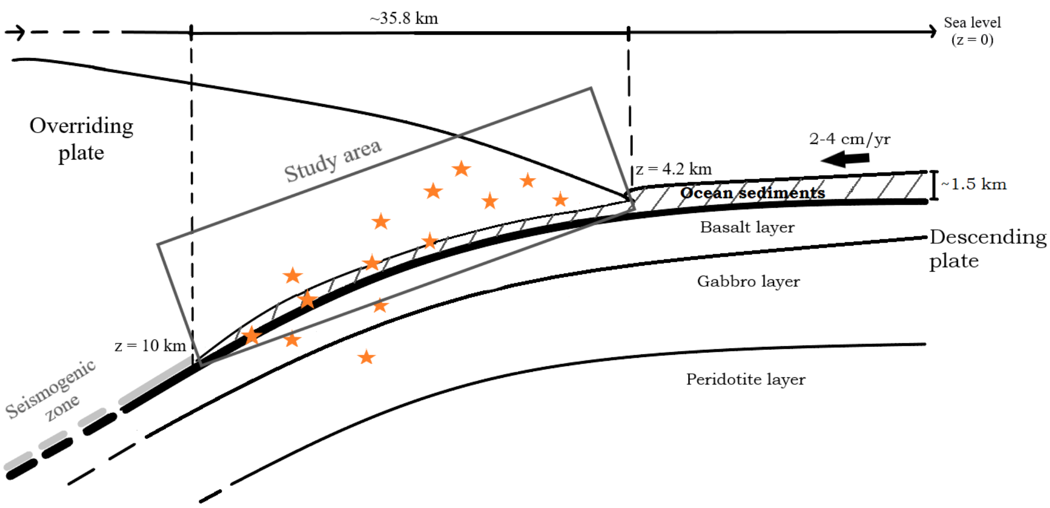

Figure 5. Illustration of the Nankai Trough subduction zone, where the square indicates the study area. The orange stars represent the hypocentres of the VLFEs. The arrows between the seismogenic zone and the up-dip region indicate compression between the accretionary prism and the locked region. The arrow at the trench axis indicates compression of the incoming sedimentary section. The largest arrow indicates the direction and rate of motion between the subducting and overriding plates. The trench axis is located approximately 4.2 km below sea level, and the edge of the study area is 10 km below sea level.

ity. The chosen threshold significantly exceeds the 1 μGal accuracy currently obtained using this technology for monitoring gas reservoirs (Ruiz et al., 2016), and in effect includes uncertainty arising from vertical seafloor movement, as well as uncertainties from oceanographic and atmospheric gravity changes. Hence, the modelling results indicate the amount of fluid increase needed to be able to produce a detectable 4D gravity signal at the seafloor above the modelled region.

Further constraining the uncertainties in gravity changes at the seafloor, and reducing this threshold on gravity, requires a detailed study of the oceanographic and atmospheric variations above the Nankai Trough, which is beyond the scope of this paper and is therefore not included in the modelling.

There is currently limited knowledge about the volumes of fluid flow related to VLFEs within the Nankai Trough accretionary prism. To relate the fluid volumes used in this study to the physical process in the rocks, we compute the corresponding porosity increase for each scenario.

Equation 4 gives the relation between the original porosity (ϕ_0) of a layer representing the fault rocks in which the mass changes are modelled, and the new porosity value (ϕ_{new}) after the pore expansion of the fault section:

$$\phi_{new} = \frac{V_0\phi_0 + dV}{V_0 + dV}. \tag{4}$$

The variable dV refers to the increased fluid volume in the area, ϕ_0 and V_0 are respectively the original porosity and volume of the affected area. For the assessment, we assume that the area A of the fault section that experiences increased fluid volume remains constant, thus $V_0 = h_0 A$ and $dV = dhA$. Hence, eq. 4 is only dependant on the thickness of the affected area and the height of the increased fluid volume. This thickness, h_0, represents the damage zone of the fault section, which can vary largely for different faults (Torabi et al., 2020). The results in Section 4 show the change in porosity of the area, given by $\Delta\phi = (\phi_{new} - \phi_0)$, where the porosities are given as fractions.

3.3.1 Scenario 1: Fluid flow along the plate interface

The first scenario models increased fluid volumes and pore expansion in the décollement along the plate interface. The hypothesis is that water expelled from the deeper rocks and sediment sections along the subducting interface migrate upwards following the pressure gradient from depths to shallow sediments. The origin of the water is likely from sediment compaction as oceanic sediments subduct (Saffer & Wallace, 2015; Tsuji et al., 2008), or possibly mineral dehydration of the deeper rocks (Saffer & Wallace, 2015).

We have limited the depth of the décollement section along the plate interface down to around 10 km, based on a study by G. F. Moore et al. (2015) anticipating an absence of subducted sediments deeper than this. Considering the important role these subducted sediments likely have in producing fluids within the subduction zone, it is assumed that the fluid will flow upwards from these depths along the interface. The lateral extent of the modelled section was constrained by the spread in locations of a cluster of VLFEs from an episode in 2016 (Nakano et al., 2016, 2018), and by possible discontinuities to the west of the DONET1 observatories indicated by seismicity in the area (Park et al., 2014). Extensive slow earthquake activity has been detected near the DONET1 observatories (Takemura et al., 2019), indicating that fluid-induced density changes can occur around this region.

Mass changes are introduced in regions of high densities, with a cutoff at 2400 kg/m^3 where sections with densities lower than this are excluded from the modelling. The assumption is that high densities are related to low porosities and corresponding low permeability which leads to pressure build-up. This density is a general average for sedimentary rocks and is therefore chosen as the limit for fluid volume changes. Park et al. (2014) estimate the average thickness of the décollement zone to be 20 m, and this thickness is used in eq. 4 to find the increase in porosity of the décollement zone.

3.3.2 Scenario 2: Fluid flow at slow earthquake locations

For the second scenario, the catalogue of VLFEs defined by Nakano et al. (2016, 2018) is used to define the locations with fluid increase. The locations of the VLFE events off the coast of the Kii Peninsula are shown in fig. 6. The episodes occurred in 2015 and 2016 and were detected by seismometers in the DONET1 network. The locations of the events were defined by Nakano et al. (2016, 2018) using centroid moment tensor inversion. The VLFEs likely occurred along thrust faults within the accretionary prism or in the oceanic crust (Nakano et al., 2016, 2018).

Rectangular prisms corresponding to the exact locations of these VLFEs are chosen for the modelling, and sections of the fault plane on which these events occur are assumed to be contained within each prism. The VLFE events have a depth uncertainty of $\pm$ 2 km (Nakano et al., 2016, 2018), introducing some uncertainties in the location of fluid changes relating to the events. Some of the events were located in the water and seafloor sections of our model, and are moved 2 km deeper relating to the uncertainty in the VLFE depths.

Empirical equations, given in eq. 5a-c, were introduced by Wells and Coppersmith (1994), relating the earthquake magnitude with length (L), width (W) and area (A) of the ruptured fault plane. These are used to define the size of the fault sections correspond-

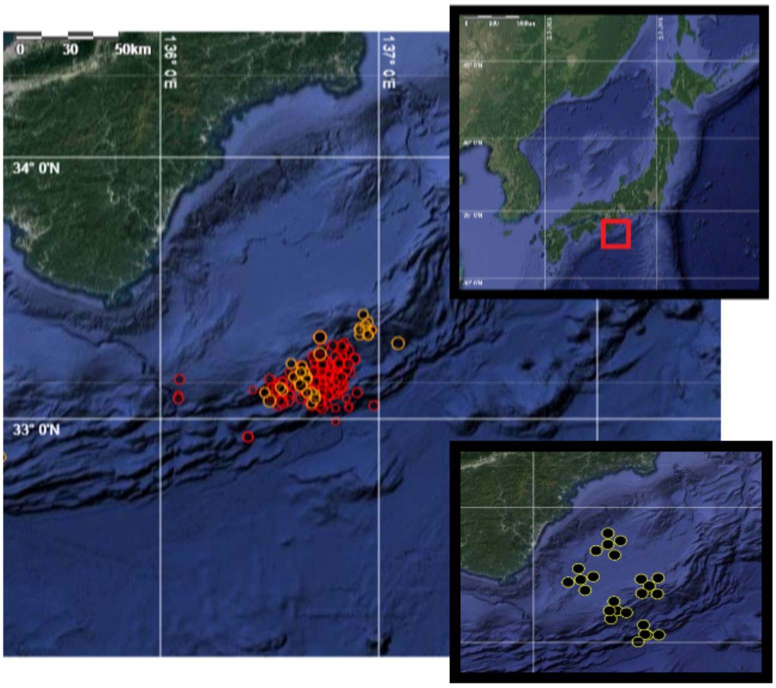

Figure 6. Epicentres for 2015 (orange) and 2016 (red) VLFEs used for the analysis in Scenario 2, located off the coast of the Kii Peninsula. The red square in upper right inset figure shows the location of the study area off the coast of Japan, while the lower right inset figure shows the location of the DONET1 observatories.

ing to the VLFEs.

$$log(W) = 0.58M_w - 2.42, \tag{5a}$$
$$log(L) = 0.41M_w - 1.61, \tag{5b}$$
$$log(A) = 0.98M_w - 3.99. \tag{5c}$$

Based on these equations, fluid volume increase in areas ranging from 0.09 - 0.17 km^2 gave good representations of individual VLFEs involved in the 2015 episode, while the range is 0.02 - 1.06 km^2 for the 2016 events. Fluid volumes are added along fault sections with the total area defined by the rupture area of the individual VLFEs.

Nakano et al. (2018) determined that the events deeper than 15 km showed strike-slip mechanisms rather than thrust faulting, indicating that they might have other triggering processes than the shallower events. Considering that some of the events in the oceanic crustal layer could also be caused by other triggering mechanisms and that our modelling focuses on the sedimentary sections in the décollement and accretionary prism, we have excluded all events deeper than the plate interface from the modelling.

The remaining events have been divided into separate periods, depending on a time-trend observed in the episodes in which earthquakes cluster at specific locations. We defined two individual areas of high earthquake activity in the 2015 episode and four areas in the 2016 episode. The events from 2015 are divided into three separate time intervals, and the events from 2016 into five intervals, to capture how the events are clustering in the different areas in time. With this time division, we aim to model the build-up of fluids in each area before the rupture of these events. The episodes are summarised in Table 2.

Table 2. Summary of VLFEs within the two catalogues used for Scenario 2. The episodes are divided into separate periods depending on the clustering of earthquakes in specific locations.

Episode	Time interval	Number of Events	Duration	Depth range (km)	Magnitude range (M_w)
2015	t_1	3	2.9 days	5-8	3.2-3.9
	t_2	14	8 hours	6-7	3-3.4
	t_3	4	1.9 days	5-7	3-3.3
2016	t_1	33	4.9 days	5-7	2.6-4.1
	t_2	88	3.2 days	5-7	2.3-3.7
	t_3	27	3.5 hours	5-8	2.4-4
	t_4	69	3.5 days	5-7	2.3-3.6
	t_5	35	5.4 days	5-7	2.2-4

4 Results and Discussion

4.1 Scenario 1: Fluid flow along the plate interface

The results for this scenario are presented together with an overview of the fault model in fig. 7. The depth contours of fig. 7a), illustrating the depth of the seafloor above the fault model, give an impression of the distance between the mass changes of the fault model and the seafloor points at which the gravity effect is computed. The 4D gravity signal for Scenario 1 is shown in fig. 7c), and Table 3 gives a summary of the fluid volume and porosity increase related to this signal, along with the size of the area where the fluid volume is built up. The mass per square kilometre indicates the amount of added mass that is required to detect the gravity signal at the seafloor. Only sections of the fault plane where the rock densities exceed 2400 kg/m^3 are used for modelling fluid changes, and the rock compressibility is assumed to be constant. The total fluid volume increase

Table 3. Results for the 4D modelling of water influx along the décollement zone with a gravity threshold of 5 μGal. The area is the section of the fault where fluid changes are modelled, and the volume is the sum of individual fluid volumes added to each subsection. The porosity value is the increase in porosity (in fraction).

	Area (km^2)	Volume increase (km^3)	Mass increase per area (kg/km^2)	$\Delta\phi$
Décollement zone	296.75	0.12	4.26×10^8	0.015

at the décollement is 0.12 km^3, distributed homogeneously over an area of 296.75 km^2. The thickness of 20 m defined for the décollement is used to estimate the porosity increase in Table 3 relating to the added fluid volume. The thickness of the actual damage zone of the plate interface may however be larger than 20 m, hence, the porosity increase estimated here could be an overestimation. The 4D gravity signal in fig. 7 indicates that the strongest signal is closest to DONET1 node B and D, and smallest near the C-node corresponding to the low-density area here. Nodes A and E are also outside of the modelled region due to the limitation of the sediment section down to 10 km, as discussed in Section 3.3.1.

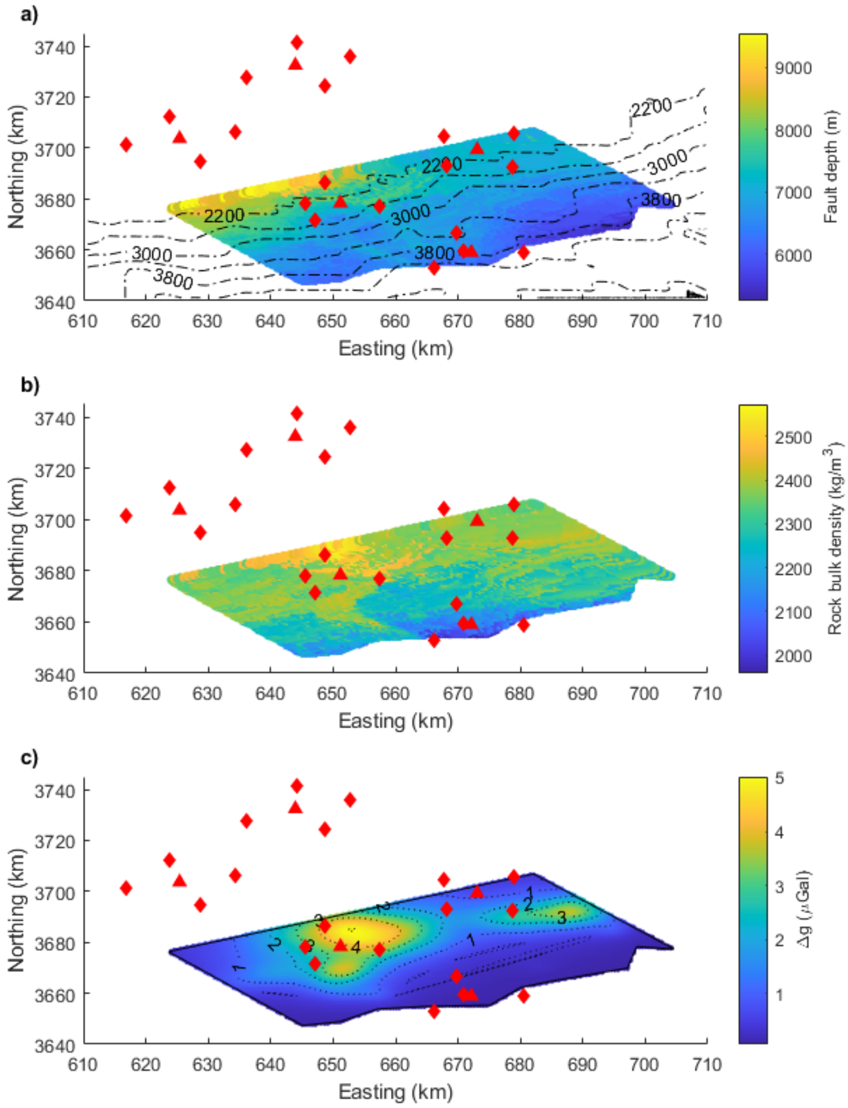

Figure 7. Results for Scenario 1. The red triangles represent the nodes of the DONET1 network, while the red diamonds are the observatory stations of the network. (a) Lateral extent and depth of the fault model representing the décollement used for the 4D gravity modelling of Scenario 1. The fault model is constrained from the trough axis and down to depths of nearly 10 km. The lateral constraint is based on VLFEs from 2016. The colours show the depth of the fault model, while the contours show the seafloor depths in the region. Depths of the seafloor and the fault model are given relative to sea level. (b) Density distribution of the fault model. Fluid build-up is modelled in regions of densities higher than 2400 kg/m^3. (c) 4D gravity results for the model. The plot includes gravity contours up to 5 μGal, while everything outside of the contours is between 0 and 1 μGal.

4.2 Scenario 2: Fluid flow at slow earthquake locations

The results of Scenario 2 indicate where fluid changes could be detected, assuming that the slow earthquakes do not necessarily occur along the plate interface, but also along other faults both within the accretionary prism and within the décollement zone. The results for both episodes are given in Table 4.

Table 4. Results for the 4D modelling of water influx in VLFE locations for the 2015 and 2016 episodes, with a gravity threshold of 5 μGal. The area is the total area of all fault planes used for the modelling, and the volume is the sum of individual fluid volumes added to each fault. The porosity value is the minimum increase in porosity (in fractions), assuming a maximum damage zone thickness of 20 m.

Episode	Time interval	Area (km^2)	Total volume change (km^3)	Mass change per area (kg/km^2)	$\Delta\phi$
2015	t_1	0.99	0.016	$1.74 \cdot 10^{10}$	0.37
	t_2	1.33	0.02	$1.55 \cdot 10^{10}$	0.32
	t_3	0.54	0.009	$1.71 \cdot 10^{10}$	0.34
2016	t_1	5.86	0.041	$7.25 \cdot 10^{9}$	0.24
	t_2	5.52	0.028	$5.27 \cdot 10^{9}$	0.09
	t_3	4.93	0.037	$7.7 \cdot 10^{9}$	0.2
	t_4	6.32	0.022	$3.65 \cdot 10^{9}$	0.05
	t_5	4.53	0.01	$2.26 \cdot 10^{9}$	0.07

For the assessment of the porosity increase, the thickness of the damage zone of the fault needs to be defined. Assuming that these faults have a smaller damage zone than the décollement of Scenario 1, the thickness could be less than 20 m. However, the actual value of h_0 to use in eq. 4 is not well constrained. The minimum porosity increase (at $h_0 = 20$ m) is given in Table 4. See Supplementary Information text S1 and figs. S1 and S2 for an analysis of the effect of varying damage zone thickness on the porosity increase relating to the given fluid volume increase. The assessment is done for both the 2015 and the 2016 clusters.

The results show that the increase in porosity must be quite large to facilitate the increased fluid volumes modelled here. An important aspect to note is that the modelled fluid volumes are concentrated within a region of the modelled asperities where the earthquakes occur, on the ruptured fault sections. As discussed in Section 3.3, the area on which the fluid volumes change is assumed to be the same as the area of the fault section. In reality, the fluid could be more spread out around the small asperities, covering a larger area even though the earthquake rupture only occurs at the asperities. Hence, the region where the fluid-induced mass changes occur is likely underestimated.

Figures 8 and 9 show the gravity signal relating to the added fluid volume for the 2015 and 2016 episodes, respectively. The area indicated in Table 4 for the two VLFE episodes refers to the total area of the individual fault planes used in the analysis; therefore this depends on the amount of VLFEs in each episode and their magnitude. The fault planes on which these VLFEs occur are located within the sandstone and limestone layers, and the surface of the upper oceanic crust. For the 2016 episode, the three periods with smaller porosity increase either include the most VLFEs (t_2 and t_4), or higher magnitude events located closer to the seafloor (t_5).

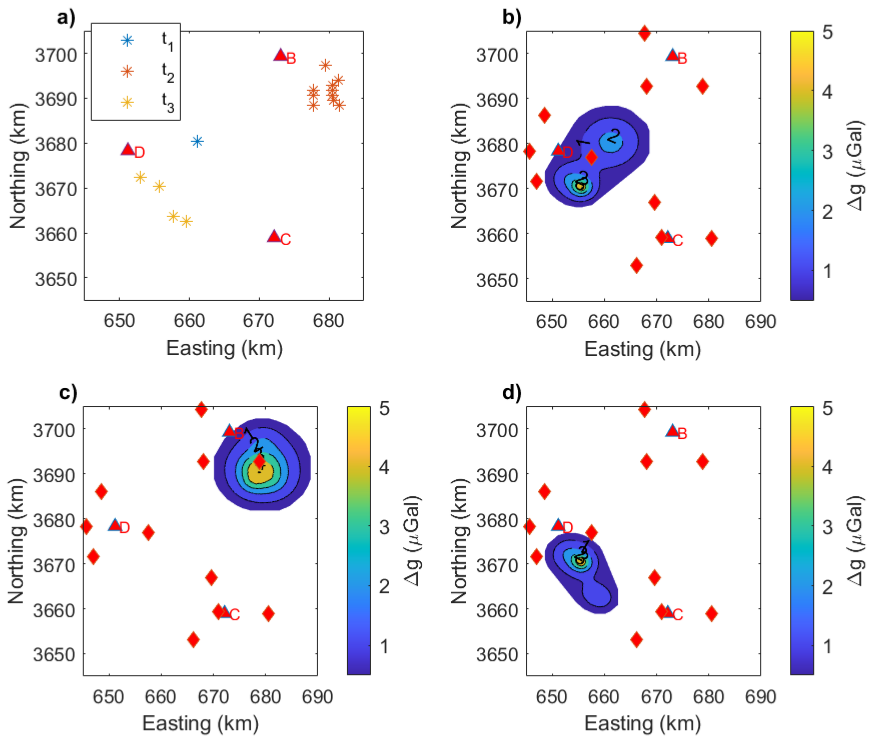

Figure 8. 4D gravity results for the VLFE episode of 2015. The DONET1 stations are shown as reference to the earthquake locations relative to the Kii Peninsula. (a) Earthquakes used in each time sequence, using the division given in Table 2. Note, two of the events in t_1 overlap with events in t_2 (the two closest to the D-node). (b) Earthquakes from time t_1. Gravity signal from $1.75 \cdot 10^{10}$ kg of increased mass per km^2. (c) Earthquakes from time t_2. Gravity signal from $1.55 \cdot 10^{10}$ kg/km^2. (d) Earthquakes from time t_3. Gravity signal from $1.71 \cdot 10^{10}$ kg/km^2.

A total of 21 events are used from the 2015 episode. These events indicate how increased fluid flow in this localised region, causing a few, relatively high magnitude VLFEs, will affect the 4D gravity signal. Less mass per area is needed in sequence t_2 to achieve a detectable gravity signal, as fluid increase occurs over a larger area. However, the events are quite deep and spread out, leading to a generally weak gravity signal from fluids relating to the 2015 episode.

The 2016 episode includes significantly more VLFEs, a total of 252 events. Therefore, these results show how a larger area could be affected by fluid build-up before slow earthquakes. More VLFEs, which have generally higher magnitudes and are more clustered together, leads to a larger total area. In result, more fault planes are used in the modelling, and less fluid is needed to be able to detect a gravity signal up to a maximum of 5 μGal. The gravity signal varies linearly with the mass change, which makes it straightforward to use the relationship between fluid volumes and 4D gravity at the seafloor here to assess the magnitude of fluid volumes also for other seafloor gravity signals.

Although the two scenarios presented here show that the results are limited to the B and D nodes of the DONET1 network, fluid may also build up near the toe of the accretionary prism, as indicated by results from an episode of slow earthquakes between December 2020 and February 2021 (Japan Meterological Agency (JAMSTEC person-

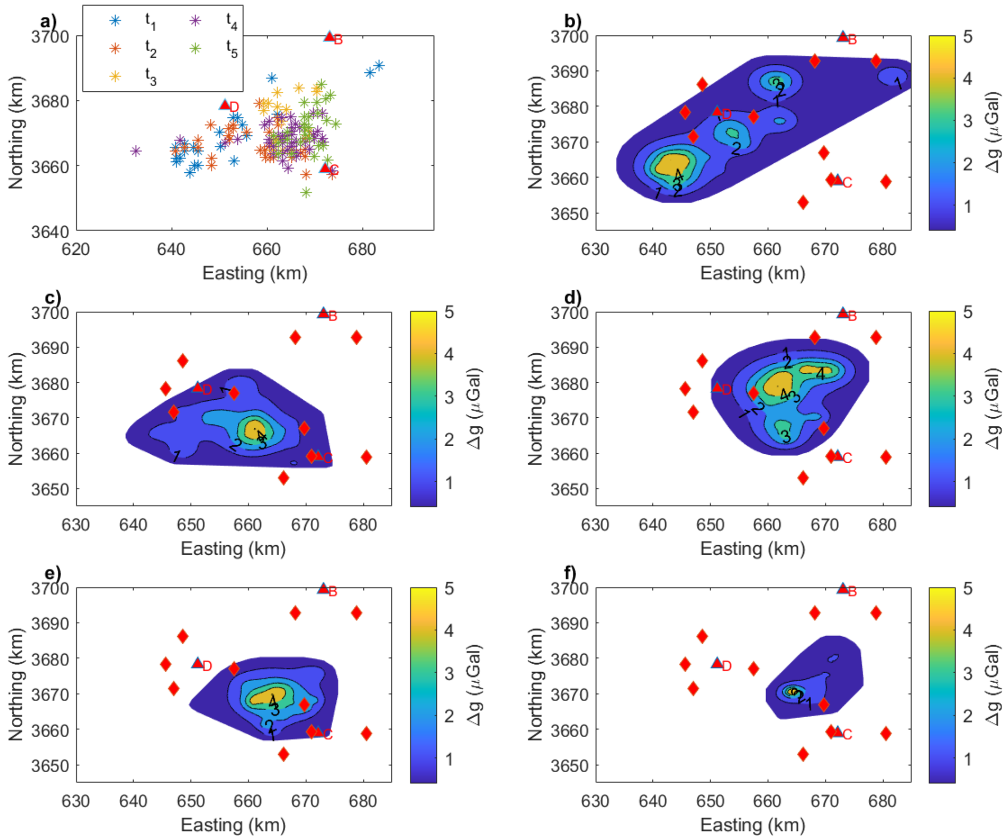

Figure 9. 4D gravity results for the VLFE episode of 2015. The DONET1 stations are shown as reference to the earthquake locations relative to the Kii Peninsula. (a) Earthquakes used in each time sequence, using the division given in Table 2. Note that two of the events in t_1 overlap with events in t_3 (the two closest to the D-node). (b) Earthquakes from time t_1. Gravity signal from $7.25 \cdot 10^9$ kg of increased mass per square km. (c) Earthquakes from time t_2. Gravity signal from $5.27 \cdot 10^9$ kg/km^2. (d) Earthquakes from time t_3. Gravity signal from $7.7 \cdot 10^9$ kg/km^2. (e) Earthquakes from time t_4. Gravity signal from $3.65 \cdot 10^9$ kg/km^2. (f) Earthquakes from time t_5. Gravity signal from $2.26 \cdot 10^9$ kg/km^2.

ell communication), 2021). Pore pressure increase detected at the observatories of the C node during this episode indicate that fluid may also build up in this area (Japan Meterological Agency (JAMSTEC personell communication), 2021), and, hence, that 4D gravity changes could also be detected closer to the prism toe.

The clusters of VLFEs studied in this scenario are assumed to be a result of episodes of fluid build-up, rupture and fluid flow between different fault sections. A study by Ottemöller et al. (2005) found clear relations between water injection at a hydrocarbon field and an induced earthquake in the overburden of the field. The injected fluid was unintentionally trapped in the overburden causing an overpressured environment, eventually leading to rupture of a M_w 4.1-4.4 event (Ottemöller et al., 2005), a clear example of how built-up fluids can lead to earthquake rupture. Various studies of black smokers at mid-ocean ridges have revealed changes in seawater temperatures experienced at vents relating to nearby earthquake activity (Sohn et al., 1998; Dziak et al., 2003), suggesting that the earthquakes may have temporarily created or opened fracture networks. The study by Dziak et al. (2003) noted a decrease in temperatures at a hydrothermal vent relating to a M_w 6.2 earthquake at the Blanco Transform, possibly indicating that the earthquake caused changes to the nearby fracture network and for a short period blocked the fluid access to this vent. Through modelling, Géli et al. (2014) show that fluid plays an important role concerning earthquakes at transform faults and discuss how these models can have implications for subduction zone earthquakes as well, where fluid may on a large scale affect the fault behaviour. These studies highlight the importance of interactions between earthquakes and fluid flow in the pore space or fracture systems in rocks.

5 Summary and Conclusion

- In this study, we provide a methodology to map the relation between mass changes due to fluid dynamics along the subduction zone at the Nankai Trough and the corresponding 4D gravity signal at the seafloor. The methodology is applied to several scenarios for fluid flow building on the assumption that slow earthquakes are triggered by built-up fluid along fault planes.
- The results show that with high accuracy 4D gravity measurements at the seafloor fairly subtle mass changes in the subsurface can be detected delineating both the spatial extent of the areas with mass build-up and the distribution of fluid flow over time.
- Scenario 1 gives an estimated fluid volume of 0.12 km^3 over an area of 296.75 km^2, corresponding to a porosity increase of 0.015, along the plate interface, leading to a gravity signal of 5 μGal at the seafloor.
- In Scenario 2 the 4D gravity response is computed for variable volumes of water increase based on the number of VLFEs used in the analysis, how large the events are and how spread out they are. The clustering of events in space and time also gives an indication of the evolution of the earthquakes in time, and therefore could indirectly show the movement of the fluid flow.
- The two scenarios have significantly different scales. Scenario 1 assumes that slow earthquakes occur along the plate interface, and fluid build-up occurs along sections of higher density rocks, assuming lower permeability here. Scenario 2 accounts for slow earthquakes on various faults in the subduction zone, only accounting for fluid volume increase along individual fault sections assumed to be involved in the rupture process.
- Our modelling results can be used to design an experimental 4D gravimetric survey, defining where expected density changes occur within the accretionary prism off the Kii Peninsula.

6 Implications for Subduction Zone Monitoring

In this study, we have investigated how seafloor gravity measurements can be used to quantify and determine the lateral extent of mass changes in the subsurface related to fluid flow processes associated with VLFEs. A framework for assessing the 4D gravity response from these fluid flow processes in the accretionary prism and subducting Philippine plate off the Kii Peninsula is developed and exemplified through two distinct scenarios.

The observed gravity signal varies linearly with the amount of mass change applied to the model. Hence, by interpreting the measured 4D gravity signal, the relations presented here can be used to determine the corresponding fluid volume change in the subsurface.

Following this study, we wish to conduct an experimental seafloor gravimetry survey at the Nankai Trough. Through this survey, the hypothesised observable density changes will be tested, which could have important implications for monitoring processes within the accretionary prism off the Kii Peninsula. For instance, if gravity changes are detected prior to the detection of slow earthquakes, the results can be used to improve our knowledge of the deformation area involved in these slow earthquake processes. If a 4D gravity signal is detected independently of any slow earthquakes, the signal could be used to estimate where fluid flow occurs in relation to steady creep. Both examples can contribute to improving our understanding of the lateral extent of processes at work within the outer reaches of the Nankai Trough subduction zone. The experiment could also contribute to delineate weakly coupled zones along the plate interface, and in return give a better definition of asperities at the Nankai Trough.

Acknowledgments

We are very thankful to JAMSTEC and Nakanishi et al. (2018) for providing access to the detailed seismic velocity structure, and for MonViro for providing the GravMod modelling tool, without which our modelling would not be possible. Our work was funded through the ASUMO project supported by Innovation Norway with Grant Number (2018/105177). The slow earthquake data from Nakano et al. (2016, 2018) was retrieved through the Slow Earthquake Database, whose research was supported by JSPS KAKENHI Grant Number JP16H06472 in Scientific Research on Innovative Areas "Science of Slow Earthquakes".

References

Agersborg, R., Hille, L., Lien, M., Lindgård, J., Ruiz, H., Vatshelle, M., et al. (2017). Density changes and reservoir compaction from in-situ calibrated 4d gravity and subsidence measured at the seafloor. In *Spe annual technical conference and exhibition.*

Ando, M. (1975). Source mechanisms and tectonic significance of historical earthquakes along the nankai trough, japan. *Tectonophysics*, *27*(2), 119–140.

Araki, E., Saffer, D. M., Kopf, A. J., Wallace, L. M., Kimura, T., Machida, Y., ... others (2017). Recurring and triggered slow-slip events near the trench at the nankai trough subduction megathrust. *Science*, *356*(6343), 1157–1160.

Ariyoshi, K., Nakata, R., Matsuzawa, T., Hino, R., Hori, T., Hasegawa, A., & Kaneda, Y. (2014). The detectability of shallow slow earthquakes by the dense oceanfloor network system for earthquakes and tsunamis (donet) in tonankai district, japan. *Marine Geophysical Research*, *35*(3), 295–310.

Barton, P. (1986). The relationship between seismic velocity and density in the continental crust—a useful constraint? *Geophysical Journal International*, *87*(1), 195–208.

Beroza, G. C., & Ide, S. (2011). Slow earthquakes and nonvolcanic tremor. *Annual review of Earth and planetary sciences*, *39*, 271–296.

Bray, C., & Karig, D. (1985). Porosity of sediments in accretionary prisms and some implications for dewatering processes. *Journal of Geophysical Research: Solid Earth*, *90*(B1), 768–778.

Bürgmann, R. (2018). The geophysics, geology and mechanics of slow fault slip. *Earth and Planetary Science Letters*, *495*, 112–134.

Calvert, A. (2011). The seismic structure of island arc crust. In *Arc-continent collision* (pp. 87–119). Springer.

Carlson, R., & Herrick, C. (1990). Densities and porosities in the oceanic crust and their variations with depth and age. *Journal of Geophysical Research: Solid Earth*, *95*(B6), 9153–9170.

Dziak, R. P., Chadwick Jr, W. W., Fox, C. G., & Embley, R. W. (2003). Hydrothermal temperature changes at the southern juan de fuca ridge associated with

mw 6.2 blanco transform earthquake. *Geology*, *31* (2), 119–122.
Engelder, T., & Price, N. (1993). Stress regimes in the lithosphere. *Engineering Geology*, *36* (3), 311–311.
Géli, L., Piau, J.-M., Dziak, R., Maury, V., Fitzenz, D., Coutellier, Q., ... Driesner, T. (2014). Seismic precursors linked to highly compressible fluids at oceanic transform faults. *Nature Geoscience*, *7* (10), 757–761.
Hirose, T., Hamada, Y., Tanikawa, W., Kamiya, N., Yamamoto, Y., Tsuji, T., ... others (2021). High fluid-pressure patches beneath the décollement: A potential source of slow earthquakes in the nankai trough off cape muroto. *Journal of Geophysical Research: Solid Earth*, e2021JB021831.
Ike, T., Moore, G. F., Kuramoto, S., Park, J.-O., Kaneda, Y., & Taira, A. (2008). Variations in sediment thickness and type along the northern philippine sea plate at the nankai trough. *Island Arc*, *17* (3), 342–357.
Ito, Y., & Obara, K. (2006). Dynamic deformation of the accretionary prism excites very low frequency earthquakes. *Geophysical Research Letters*, *33* (2).
Ito, Y., Obara, K., Shiomi, K., Sekine, S., & Hirose, H. (2007). Slow earthquakes coincident with episodic tremors and slow slip events. *Science*, *315* (5811), 503–506.
JAMSTEC. (2019). *Nankai trough seismogenic zone experiment.* Retrieved 2019-10-18, from https://www.jamstec.go.jp/chikyu/e/nantroseize/
Japan Meterological Agency (JAMSTEC personell communication). (2021). *Recent seismic and crustal movement activities around the nankai trough.* Retrieved 2021-07-12, from https://www.jma.go.jp/jma/press/2102/05c/mate01_4.pdf
Kanamori, H. (1971). Great earthquakes at island arcs and the lithosphere. *Tectonophysics*, *12* (3), 187–198.
Kano, M., Aso, N., Matsuzawa, T., Ide, S., Annoura, S., Arai, R., ... others (2018). Development of a slow earthquake database. *Seismological Research Letters*, *89* (4), 1566–1575.
Kawaguchi, K., Kaneko, S., Nishida, T., & Komine, T. (2015). Construction of the donet real-time seafloor observatory for earthquakes and tsunami monitoring. In P. Favali, L. Beranzoli, & A. De Santis (Eds.), *Seafloor observatories: A new vision of the earth from the abyss* (p. 211-228). Springer Science & Business Media.
Kearey, P., Klepeis, K. A., & Vine, F. J. (2009). *Global tectonics.* John Wiley & Sons.
Kehew, A. E. (1994). *Geology for engineers and environmental scientists (2nd edition).* Prentice Hall. Retrieved from https://www.xarg.org/ref/a/0133035387/
Kinoshita, M., Tobin, H., Ashi, J., Kimura, G., Lallemant, S., Screaton, E., & Curewitz, D. (2012). Data report: clay mineral assemblages from the nankai trough accretionary prism and the kumano basin, iodp expeditions 315 and 316, nantroseize stage 1. In *Proc. iodp— volume* (Vol. 314, p. 2).
Kodaira, S., Iidaka, T., Kato, A., Park, J.-O., Iwasaki, T., & Kaneda, Y. (2004). High pore fluid pressure may cause silent slip in the nankai trough. *Science*, *304* (5675), 1295–1298.
Lay, T., & Kanamori, H. (1981). An asperity model of large earthquake sequences.
Linde, A. T., & Sacks, I. S. (2002). Slow earthquakes and great earthquakes along the nankai trough. *Earth and Planetary Science Letters*, *203* (1), 265–275.
Ludwig, W., Nafe, J., & Drake, C. (1970). *The sea, vol. 4, part 1.* Wiley-Interscience London.
Mavko, G., Mukerji, T., & Dvorkin, J. (2009). *The rock physics handbook: Tools for seismic analysis of porous media.* Cambridge university press.
MonViro. (2019). *GravMod.* In-house software. Bergen, Norway.
Moore, G. F., Boston, B. B., Strasser, M., Underwood, M. B., & Ratliff, R. A.

(2015). Evolution of tectono-sedimentary systems in the kumano basin, nankai trough forearc. *Marine and Petroleum Geology*, *67*, 604–616.

Moore, J. C., & Vrolijk, P. (1992). Fluids in accretionary prisms. *Reviews of Geophysics*, *30*(2), 113–135.

Mussett, A. E., & Khan, M. A. (2000). *Looking into the earth: an introduction to geological geophysics*. Cambridge University Press.

Nakanishi, A., Takahashi, N., Park, J.-O., Miura, S., Kodaira, S., Kaneda, Y., … Nakamura, M. (2002). Crustal structure across the coseismic rupture zone of the 1944 tonankai earthquake, the central nankai trough seismogenic zone. *Journal of Geophysical Research: Solid Earth*, *107*(B1), EPM–2.

Nakanishi, A., Takahashi, N., Yamamoto, Y., Takahashi, T., Citak, S. O., Nakamura, T., … Kaneda, Y. (2018). Three-dimensional plate geometry and p-wave velocity models of the subduction zone in sw japan: Implications for seismogenesis. *Geology and Tectonics of Subduction Zones: A Tribute to Gaku Kimura*, *534*, 69.

Nakano, M., Hori, T., Araki, E., Kodaira, S., & Ide, S. (2018). Shallow very-low-frequency earthquakes accompany slow slip events in the nankai subduction zone. *Nature communications*, *9*(1), 984.

Nakano, M., Hori, T., Araki, E., Takahashi, N., & Kodaira, S. (2016). Ocean floor networks capture low-frequency earthquake event. *Eos*, *97*.

Noda, A., Saito, T., & Fukuyama, E. (2018). Slip-deficit rate distribution along the nankai trough, southwest japan, with elastic lithosphere and viscoelastic asthenosphere. *Journal of Geophysical Research: Solid Earth*, *123*(9), 8125–8142.

Obara, K., & Ito, Y. (2005). Very low frequency earthquakes excited by the 2004 off the kii peninsula earthquakes: A dynamic deformation process in the large accretionary prism. *Earth, Planets and Space*, *57*(4), 321–326.

Okino, K., Shimakawa, Y., & Nagaoka, S. (1994). Evolution of the shikoku basin. *Journal of geomagnetism and geoelectricity*, *46*(6), 463–479.

Ottemöller, L., Nielsen, H., Atakan, K., Braunmiller, J., & Havskov, J. (2005). The 7 may 2001 induced seismic event in the ekofisk oil field, north sea. *Journal of Geophysical Research: Solid Earth*, *110*(B10).

Ozawa, S., Nishimura, T., Suito, H., Kobayashi, T., Tobita, M., & Imakiire, T. (2011). Coseismic and postseismic slip of the 2011 magnitude-9 tohoku-oki earthquake. *Nature*, *475*(7356), 373–376.

Panet, I., Bonvalot, S., Narteau, C., Remy, D., & Lemoine, J.-M. (2018). Migrating pattern of deformation prior to the tohoku-oki earthquake revealed by grace data. *Nature Geoscience*, *11*(5), 367.

Park, J.-O., Naruse, H., & Bangs, N. L. (2014). Along-strike variations in the nankai shallow décollement properties and their implications for tsunami earthquake generation. *Geophysical Research Letters*, *41*(20), 7057–7064.

Ruff, L., & Kanamori, H. (1983). Seismic coupling and uncoupling at subduction zones. *Tectonophysics*, *99*(2-4), 99–117.

Ruiz, H., Agersborg, R., Hille, L., Lindgård, J. E., Lien, M., & Vatshelle, M. (2016). Monitoring offshore reservoirs using 4d gravity and subsidence with improved tide corrections. In *Seg technical program expanded abstracts 2016* (pp. 2946–2950). Society of Exploration Geophysicists.

Ruiz, H., Lien, M., Vatshelle, M., Alnes, H., Haverl, M., & Sørensen, H. (2020). Monitoring the snøhvit gas field using seabed gravimetry and subsidence. In *Seg technical program expanded abstracts 2020* (pp. 3768–3772). Society of Exploration Geophysicists.

Saffer, D. M., & Wallace, L. M. (2015). The frictional, hydrologic, metamorphic and thermal habitat of shallow slow earthquakes. *Nature Geoscience*, *8*(8), 594.

Satake, K. (2015). Geological and historical evidence of irregular recurrent earthquakes in japan. *Philosophical Transactions of the Royal Society A: Mathemat-*

ical, Physical and Engineering Sciences, *373*(2053), 20140375.
Schön, J. H. (2015). *Physical properties of rocks: Fundamentals and principles of petrophysics* (Vol. 65). Elsevier.
Screaton, E., Kimura, G., Curewitz, D., Moore, G., Chester, F., Fabbri, O., ... others (2009). Interactions between deformation and fluids in the frontal thrust region of the nantroseize transect offshore the kii peninsula, japan: Results from iodp expedition 316 sites c0006 and c0007. *Geochemistry, Geophysics, Geosystems*, *10*(12).
Seno, T., Stein, S., & Gripp, A. E. (1993). A model for the motion of the philippine sea plate consistent with nuvel-1 and geological data. *Journal of Geophysical Research: Solid Earth*, *98*(B10), 17941–17948.
Shelly, D. R., Beroza, G. C., Ide, S., & Nakamula, S. (2006). Low-frequency earthquakes in shikoku, japan, and their relationship to episodic tremor and slip. *Nature*, *442*(7099), 188.
Sohn, R. A., Fornari, D. J., Von Damm, K. L., Hildebrand, J. A., & Webb, S. C. (1998). Seismic and hydrothermal evidence for a cracking event on the east pacific rise crest at 9 50′ N. *Nature*, *396*(6707), 159–161.
Stein, S., Wysession, M., & Houston, H. (2003). Books-an introduction to seismology, earthquakes, and earth structure. *Physics Today*, *56*(10), 65–72.
Sugimura, A., & Uyeda, S. (1973). Developments in geotectonics 3: Island arcs, japan and its environs.
Taira, A., Ashi, J., & Byrne, T. (1992). *Photographic atlas of an accretionary prism: geologic structures of the shimanto belt, japan* (Tech. Rep.).
Taira, A., Okada, H., Whitaker, J., & Smith, A. (1982). The shimanto belt of japan: cretaceous-lower miocene active-margin sedimentation. *Geological Society, London, Special Publications*, *10*(1), 5–26.
Takemura, S., Matsuzawa, T., Noda, A., Tonegawa, T., Asano, Y., Kimura, T., & Shiomi, K. (2019). Structural characteristics of the nankai trough shallow plate boundary inferred from shallow very low frequency earthquakes. *Geophysical Research Letters*, *46*(8), 4192–4201.
The Headquarters for Earthquake Research Promotion. (2020). *Monthly reports on evaluation of seismic activities in japan.* Retrieved 2020-04-06, from `https://www.jishin.go.jp/main/index-e.html`
Tomoda, Y. (2010). Gravity at sea—a memoir of a marine geophysicist—. *Proceedings of the Japan Academy, Series B*, *86*(8), 769–787.
Tonegawa, T., Araki, E., Kimura, T., Nakamura, T., Nakano, M., & Suzuki, K. (2017). Sporadic low-velocity volumes spatially correlate with shallow very low frequency earthquake clusters. *Nature communications*, *8*(1), 2048.
Torabi, A., Ellingsen, T., Johannessen, M., Alaei, B., Rotevatn, A., & Chiarella, D. (2020). Fault zone architecture and its scaling laws: where does the damage zone start and stop? *Geological Society, London, Special Publications*, *496*(1), 99–124.
Tsuboi, S., & Nakamura, T. (2013). Sea surface gravity changes observed prior to march 11, 2011 tohoku earthquake. *Physics of the Earth and Planetary Interiors*, *221*, 60–65.
Tsuji, T., Tokuyama, H., Costa Pisani, P., & Moore, G. (2008). Effective stress and pore pressure in the nankai accretionary prism off the muroto peninsula, southwestern japan. *Journal of Geophysical Research: Solid Earth*, *113*(B11).
Underwood, M. B., & Song, C. (2016). Data report: Clay mineral assemblages in cuttings from hole c0002f, iodp expedition 338, upper nankai trough accretionary prism. *Strasser, M., Dugan, B., Kanagawa, K., Moore, GF, Toczko, S., Maeda, L. and the Expedition 338 Scientists, Proc. IODP*, *338*.
Wells, D. L., & Coppersmith, K. J. (1994). New empirical relationships among magnitude, rupture length, rupture width, rupture area, and surface displacement. *Bulletin of the seismological Society of America*, *84*(4), 974–1002.

Yokota, Y., Ishikawa, T., Watanabe, S.-i., Tashiro, T., & Asada, A. (2016). Seafloor geodetic constraints on interplate coupling of the nankai trough megathrust zone. *Nature*, *534*(7607), 374.